

Engineering Water-Lotus-like Iridium–Cobalt Carbonate Hydroxides on Plasma-Treated Carbon Fibers for Enhanced Electrocatalytic Oxygen Evolution

Ying Xie, Jinfeng Qiu, Guangliang Chen,* Yingchun Guo, Peisong Tang, and Bin He



Cite This: *Inorg. Chem.* 2024, 63, 15467–15476



Read Online

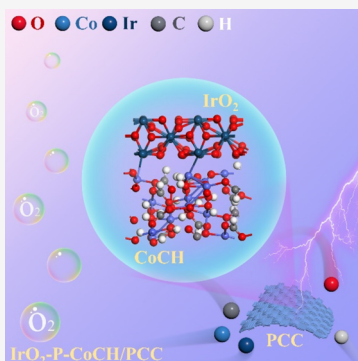
ACCESS |

Metrics & More

Article Recommendations

Supporting Information

ABSTRACT: The sluggish kinetics of the oxygen evolution reaction (OER) in alkaline water electrolysis remains a significant challenge for developing high-efficiency electrocatalytic systems. In this study, we present a three-dimensional, micrometer-sized iridium oxide (IrO_2)-decorated cobalt carbonate hydroxide ($\text{IrO}_2\text{-P-CoCH}$) electrocatalyst, which is engineered *in situ* on a carbon cloth (CC) substrate pretreated with atmospheric-pressure dielectric barrier discharge (DBD) plasma (PCC). The electrocatalyst features petal-like structures composed of nanosized rods, providing abundant reactive areas and sites, including the oxygen vacancy caused by the air–DBD plasma. As a result, the $\text{IrO}_2\text{-P-CoCH}/\text{PCC}$ electrocatalyst demonstrates an outstanding OER performance, with overpotentials of only 190 and 300 mV required to achieve current densities of 10 mA cm^{-2} (j_{10}) and 300 mA cm^{-2} (j_{300}), respectively, along with a low Tafel slope of 48.1 mV dec^{-1} in 1.0 M KOH . Remarkably, benefiting from rich active sites exposed on the $\text{IrO}_2\text{-P-CoCH}$ (Ir) heterostructure, the synergistic effect between IrO_2 and CoCH enhances the charge delivery rates, and the $\text{IrO}_2\text{-P-CoCH}/\text{PCC}$ exhibits a superior electrocatalytic activity at a high current density ($300 \text{ mV}/j_{300}$) compared to the commercial benchmarked RuO_2/PCC ($470 \text{ mV}/j_{300}$). Furthermore, the $\text{IrO}_2\text{-P-CoCH}/\text{PCC}$ electrocatalyst shows exceptional OER stability, with a mere 1.3% decrease with a current density of j_{10} for 100 h testing, surpassing most OER catalysts based on CC substrates. This work introduces a novel approach for designing high-performance OER electrocatalysts on flexible electrode substrates.



1. INTRODUCTION

The consumption of fossil fuels has led to numerous critical issues, including environmental pollution, energy scarcity, and global warming. Transitioning to green and clean energy sources is vital to alleviate the energy crisis and achieve renewable energy targets and carbon neutrality.^{1,2} Hydrogen, with its high energy density and renewability, is considered as one of the most promising alternative energy sources.^{3,4} Electrochemical water splitting, utilizing renewable electricity for hydrogen production, presents an ideal and sustainable method.⁵ This process involves two half-reactions: the hydrogen evolution reaction (HER) and the oxygen evolution reaction (OER). However, the slow kinetics of OER, a four-electron transfer process ($4\text{OH}^- \rightarrow 2\text{H}_2\text{O} + 4\text{e}^- + \text{O}_2$), results in an actual oxidation potential significantly higher than the theoretical potential (~1.23 V), posing a major obstacle in water splitting.⁶

Designing efficient electrocatalysts to lower the high overpotential of the OER is a key challenge in the field of electrocatalysis. Iridium-based materials exhibit high catalytic activities for both HER and OER.^{7–9} However, the high cost and scarcity of noble metals hinder their industrial applications.¹⁰ Combining Ir with other materials can enhance electrocatalytic activity and stability while reducing costs.^{11,12} Transition metal-based electrocatalysts, particularly those

involving cobalt hydroxide, have garnered significant attention for their excellent electrochemical performance in water splitting.^{13,14} Cobalt hydroxide carbonate (CoCH) serves as a primary precursor for cobalt-based catalysts due to its properties similar to Co(OH)_2 and its morphology that provides a large reactive area and straightforward preparation. Nevertheless, the low intrinsic activity and poor electrical conductivity of CoCH limit its application in electrocatalysis.^{15–17}

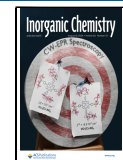
To address these limitations, it is crucial to enhance the electrocatalytic performance of CoCH by incorporating highly active elements and utilizing conductive substrates. Carbon cloth (CC) is an ideal substrate due to its large specific surface area, excellent electrical conductivity, and corrosion resistance in alkaline electrolytes. Its low cost and flexibility make it an attractive material for developing flexible electrodes. However, the hydrophobic nature and the smooth surface of carbon

Received: June 23, 2024

Revised: August 1, 2024

Accepted: August 1, 2024

Published: August 6, 2024



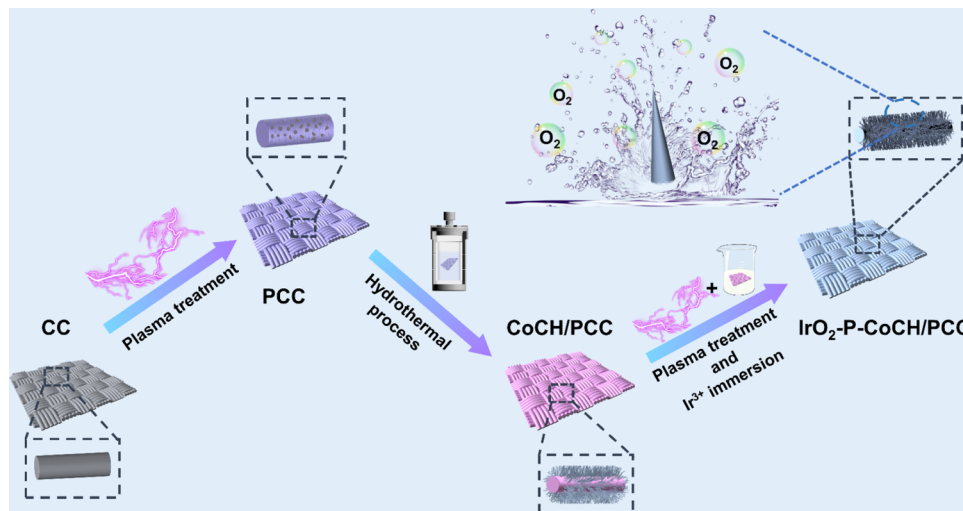


Figure 1. Schematic diagram for in situ engineering $\text{IrO}_2\text{-P-CoCH/PCC}$.

fibers hinder the adhesion of catalysts, posing a challenge for stable CC-based electrocatalysts.^{16–20}

Strategies to enhance catalyst performance typically involve the increased specific surface area, enriched reactive sites, and doped heteroatoms to tune electron states.^{17–19} In this study, we employed a two-step dielectric barrier discharge (DBD) plasma treatment to modify the CC surface for increasing the combining intensity between CC and catalyst as well as etching the CoCH for creating oxygen vacancy and optimizing the IrO_2 decoration. Therefore, the resulting cobalt carbonate hydroxide decorated by IrO_2 on plasma-treated carbon cloth ($\text{IrO}_2\text{-P-CoCH/PCC}$) demonstrates an exceptional electrocatalytic performance in an alkaline medium. The voltages required to achieve current densities of j_{10} and j_{100} for the $\text{IrO}_2\text{-P-CoCH/PCC}||\text{IrO}_2\text{-P-CoCH/PCC}$ cell system are 1.52 and 1.67 V, respectively, outperforming most reported CC-based catalysts. This work introduces a novel approach for in situ engineering of high-efficiency and flexible electrocatalysts for water splitting applications.

2. EXPERIMENTAL SECTION

2.1. Chemicals and Reagents. Carbon cloth (CC) was purchased from Suzhou Shengeruo Technology Co. Ethanol ($\text{C}_2\text{H}_6\text{O}$, 95%), acetone, hydrochloric acid (HCl), deionized water, cobalt nitrate hexahydrate ($(\text{Co}(\text{NO}_3)_2\cdot 6\text{H}_2\text{O})$), iridium trichloride ($(\text{IrCl}_3\cdot x\text{H}_2\text{O})$), ammonium fluoride (NH_4F , 98%), urea, potassium hydroxide (KOH), and ruthenium dioxide (RuO_2 , 99.9%) were supplied by Hangzhou Minling Chemical Instrument Co. Note that all chemical reagents were of analytical purity.

2.2. Synthesis of CoCH/PCC. Carbon cloth (CC, $1 \times 2 \text{ cm}^2$) was washed with acetone and HCl (3 M) for 30 min by ultrasonication, followed by rinsing with plenty of ethanol and deionized water. The cleaned CC was dried in an oven at 50 °C for 2 h, and then both sides of CC were treated by an air–DBD plasma with a power of 50 W for 5 min (PCC). Meanwhile, 2 mmol of $\text{Co}(\text{NO}_3)_2\cdot 6\text{H}_2\text{O}$, 10 mmol of urea, and 4 mmol of NH_4F were dissolved in 25 mL of deionized water and stirred with a magnetic stirrer for 20 min to obtain a homogeneous solution. Subsequently, the PCC and the mixed solution were transferred to an autoclave with a Teflon liner and kept at 120 °C in an air-drying device for 6 h. After the reaction, the resulting sample (CoCH/PCC) was washed three times with ethanol and deionized water, respectively. Finally, the CoCH/PCC was dried in an oven at 50 °C for 2 h. To obtain an optimized catalyst, different reactive parameters were also investigated.

2.3. Fabrication of $\text{IrO}_2\text{-P-CoCH/PCC}$. The synthesized CoCH/PCC was cut into a square piece ($1 \times 1 \text{ cm}^2$) and modified with DBD plasma with a power of 50 W for 3 min, which was named P-CoCH/PCC. Meanwhile, 0.01 g of iridium trichloride hydrate ($(\text{IrCl}_3\cdot x\text{H}_2\text{O})$) was entirely dissolved in 10 mL of deionized water, and the P-CoCH/PCC was immersed in the reactive solution at room temperature (25 °C) for 8 h. After the reaction, the sample was washed three times with ethanol and deionized water, respectively, and quickly dried for 2 h in an oven with a temperature of 50 °C to obtain the final catalyst of $\text{IrO}_2\text{-P-CoCH/PCC}$. It should be noted that the weight of $\text{IrO}_2\text{-P-CoCH/PCC}$ loaded on the PCC surface was about $2.97 \text{ mg}\cdot\text{cm}^{-2}$. For comparison, the catalysts of $\text{IrO}_2\text{-P-CoCH/PCC}$ with different treating times of DBD plasma, as well as the $\text{IrO}_2\text{-CoCH/PCC}$ without plasma modification, were prepared.

2.4. Material Characterization. The physical structures of the obtained samples were characterized by using a field-emission scanning electron microscope (FE-SEM, JSM-6700F, Japan) and a transmission electron microscope (TEM, model JSM-2100, JEOL, Japan). Simultaneously, energy-dispersive X-ray spectra (EDS) of SEM and TEM were used to indicate the element distribution on the catalyst surface. The changes of valence states and crystalline phases of catalysts before and after the OER were analyzed by using X-ray diffraction (XRD, Thermo Fisher Scientific) and X-ray photoelectron spectroscopy (XPS, K-Alpha). The electron paramagnetic resonances (EPR) spectra were measured on a Bruker A300 spectrometer (Germany) for detecting the oxygen vacancy (O_v). Meanwhile, the inductively coupled plasma emission spectrometer (ICP-OES) was used to determine the weight percentage of Co and Ir in the synthesized catalysts, and the X-ray source was operated at 300 W (Al $\text{K}\alpha$: 1486.6 eV) (OES, Agilent 720/730).

2.5. Electrochemical Measurements. The electrochemical properties of the catalysts were all tested by an electrochemical workstation (Model: CHI 660E, Shanghai Chenhua Instrument Co., Ltd.) in 1 M KOH at 25 °C. The electrochemical data were obtained from a conventional three-electrode system, where the $\text{IrO}_2\text{-P-CoCH/PCC}$, carbon rod, and saturated calomel electrode (SCE) acted as the working electrode, reference electrode, and counter electrode, respectively. Meanwhile, for normalization, all tested data were converted to the relative reversible hydrogen electrode (RHE) according to the Nernst equation ($E_{\text{vs RHE}} = E_{\text{vs Hg/HgO}} + 0.095 + 0.059 \times \text{pH}$). In the measuring process, the samples were cut into $1 \times 0.5 \text{ cm}^2$ (test area: $0.5 \times 0.5 \text{ cm}^2$), and CV cycles were performed for 50 times at a scan rate of 50 mV s^{-1} to activate catalysts. Then, a linear scanning voltammetry (LSV) test was performed with a frequency of 1 mV s^{-1} and a voltage range of 0 to 1.4 V. Noticeably, according to the equation: $E_{\text{Corrected}} = E_{\text{Raw}} - IR_s$, the ohmic resistance of the solution compensates 90% iR -compensation for the polarization

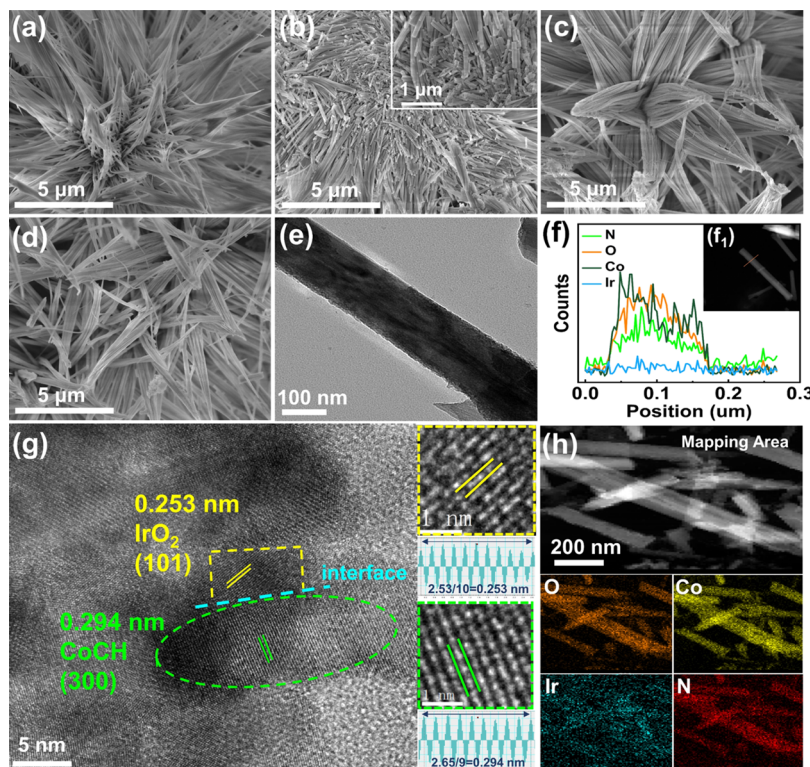


Figure 2. Physicochemical structures of the catalysts detected by SEM (a–d) and TEM (e–h). (a) CoCH/PCC, (b) P-CoCH/PCC, (c) IrO₂-P-CoCH/PCC, (d) IrO₂-CoCH/PCC, (e) low-resolution TEM of single IrO₂-P-CoCH nanocone, (f) the element distribution across the nanocone (f₁), (g) high-resolution TEM images of IrO₂-P-CoCH, and (h) the elemental maps of IrO₂-P-CoCH nanocones.

curve of the OER. It should be noted that the electrochemical impedance spectra (ESI) and electrochemical surface area (ECSA) of the catalysts were detected with similar methods reported in our former work.²⁰ At the same time, the amount of O₂ produced by the resulting catalyst electrodes was obtained by the drainage method, and the electrocatalytic sustainability of IrO₂-P-CoCH/PCC was assessed by the decay intensity of current density of j_{10} or j_{100} for 100 h.

2.6. Theoretical Simulations. All of the calculations were performed in the framework of the density functional theory with the projector-augmented plane-wave method, as implemented in the VASP.²¹ The generalized gradient approximation proposed by Perdew, Burke, and Ernzerhof was selected for the exchange-correlation potential.²² The van der Waals interaction was described by the DFT-D3 approach.²³ The cutoff energy for the plane wave was set to 400 eV. The energy criterion was set to 10^{-4} eV in the iterative solution of the Kohn–Sham equation. A vacuum layer of 15 Å was added perpendicular to the sheet to avoid artificial interaction between periodic images. The Brillouin zone integration was performed using a $2 \times 2 \times 1$ k-mesh. All of the structures were relaxed until the residual forces on the atoms declined to less than 0.02 eV/Å. In addition, to evaluate the OER activity, the Gibbs free energy of intermediate adsorbed on the catalyst was considered, and the calculation method follows our previously published works.²⁴

3. RESULTS AND DISCUSSION

3.1. Structural Characterization of Electrocatalysts. As illustrated in Figure 1, the IrO₂-P-CoCH/PCC electrocatalyst is synthesized by using a combination of two-plasma modification processes and a conventional hydrothermal method. Initially, both sides of cleaned carbon cloth (CC) are treated with a two-plate dielectric barrier discharge (DBD) plasma system to create a hydrophilic and roughened substrate (PCC) (Figure S1). As shown in Figure S1b, many

micro(nano)sized holes are formed on the PCC surface, which significantly enhances the bonding strength between the carbon fibers and the catalyst. Additionally, some polar groups are grafted on the PCC surface under the function of air–DBD plasma, and the improved surface wettability of PCC (Figure S1d) increases the nucleation density of the reactive precursor, leading to a higher growth rate of the electrocatalyst on the carbon fiber surface. These modifications are crucial for boosting the electrocatalytic performance of the resulting electrode materials.²⁵ The optimized PCC substrate was determined by evaluating the OER performance of samples treated under various DBD parameters (Figure S2). Subsequently, CoCH was synthesized on the PCC surface via a straightforward hydrothermal reaction, resulting in CoCH/PCC. To maximize the OER activity of CoCH/PCC, different reaction times and temperatures were tested (Figures S3 and S4), leading to the identification of optimal conditions: a temperature of 120 °C and a reaction time of 6 h.

To increase the density of active sites and polar groups on the catalyst surface, CoCH/PCC is treated with air–DBD plasma (P-CoCH/PCC). This treatment introduces new functional groups (e.g., C=O, C–O, –COOH), etching microsized holes, and creating oxygen vacancy on the material surface,²⁶ which facilitate the absorption of Ir ions and cause a high OER performance. Figure S5 and S6 illustrates the effects of Ir³⁺ concentration and DBD treatment time on the OER activity of P-CoCH/PCC decorated by IrO₂ (IrO₂-P-CoCH/PCC). The optimized Ir content and etching morphology result in the largest reactive area. Notably, some Co²⁺ ions on the catalyst surface are replaced by Ir³⁺ during the soaking process, and plasma etching effectively increases the Ir content anchored on the P-CoCH/PCC surface. This is evidenced by

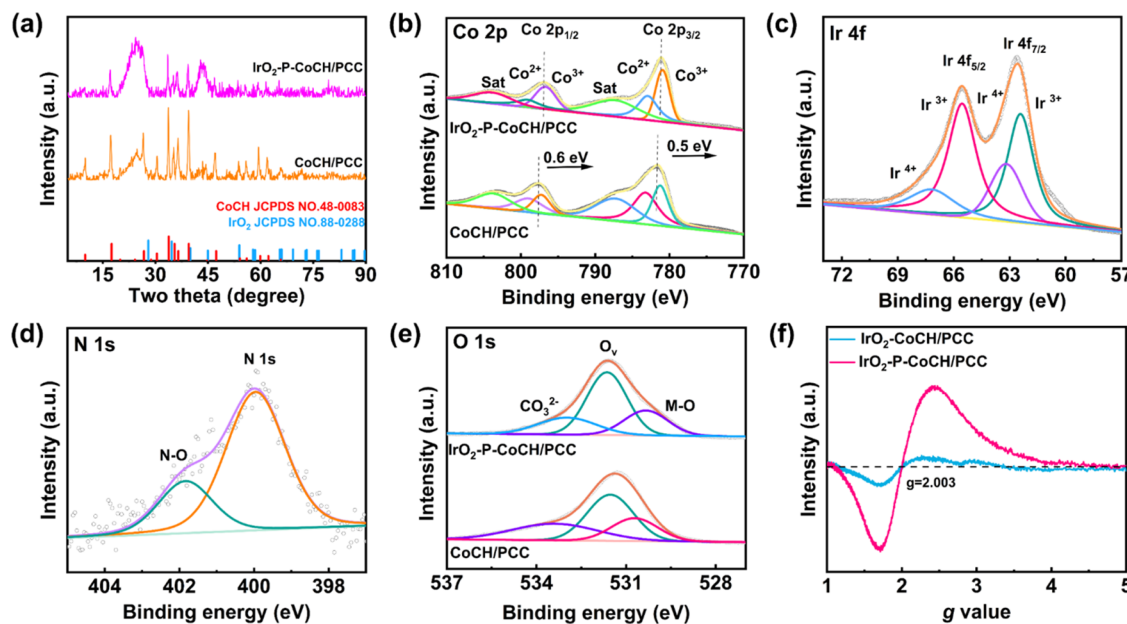


Figure 3. (a) XRD spectra of different samples and the XPS spectrum of $\text{IrO}_2\text{-P-CoCH}/\text{PCC}$ and CoCH/PCC ; the high-resolution spectra of (b) Co 2p, (c) Ir 4f, (d) N 1s, and (e) O 1s; (f) EPR spectra.

the higher Ir mass in $\text{IrO}_2\text{-P-CoCH}/\text{PCC}$ (0.35 wt %) compared to $\text{IrO}_2\text{-CoCH}/\text{PCC}$ (0.28 wt %) under the same reaction conditions (Table S1).

The morphology of the materials is closely related to their electrocatalytic performance. Figure 2 and S7 shows the surface profiles of CoCH/PCC , $\text{P-CoCH}/\text{PCC}$, $\text{IrO}_2\text{-P-CoCH}/\text{PCC}$, and $\text{IrO}_2\text{-CoCH}/\text{PCC}$, respectively. For the original CoCH/PCC (Figure 2a), the flower-like petals are composed of numerous nanocones, enhancing the electrocatalytic area of the catalyst. To create a higher density of reactive sites for absorbing Ir ions, CoCH/PCC is treated with DBD plasma, resulting in some nanocones being broken or etched by high-energy ions (Figure 2b). The optimized $\text{IrO}_2\text{-P-CoCH}/\text{PCC}$ (Figure 2c) exhibits larger nanocone dimensions compared to CoCH and $\text{IrO}_2\text{-CoCH}/\text{PCC}$ (Figure 2d). The micro-sized petals of $\text{IrO}_2\text{-P-CoCH}$ significantly improve the electrocatalytic stability of the catalyst. Low-resolution TEM images (Figure 2e) reveal that the bottom-part diameter of the nanocones is approximately 150 nm. As depicted in Figure 2f, the elements detected across the nanocones include Co, O, and N, with a small amount of Ir, which aligns with the XPS results presented later. The N element on the nanocone surface is primarily derived from the doping process during the DBD plasma treatment. Figure 2g shows the high-resolution TEM (HRTEM) image of $\text{IrO}_2\text{-P-CoCH}/\text{PCC}$, where the exposed lattice spacings of 0.253 and 0.294 nm correspond to the IrO_2 (101) and CoCH (300) crystal planes, respectively. The achieved rich interfaces can be used to effectively tune the charge transfer rate between the two phases, and then, the electrocatalytic activity of $\text{IrO}_2\text{-P-CoCH}$ can be enhanced greatly. These high-index planes are typically associated with high electrocatalytic activity.³⁰ Additionally, the selected area electron diffraction (SAED) patterns confirm the single-crystal nature of $\text{IrO}_2\text{-P-CoCH}/\text{PCC}$ (Figure S8), indicating that the decorated IrO_2 does not alter the primary crystal structure of CoCH . Figure 2h presents the high-angle annular dark-field scanning transmission electron microscopy (HAADF-STEM) image of $\text{IrO}_2\text{-P-CoCH}$, showing a uniform distribution of Co,

Ir, N, and O elements on the nanocone surface. The low Ir content (1.04%, Figure S9) not only sustains high OER activity but also helps reduce the overall cost of the catalyst.

As shown in Figure 3a, the crystal structure of synthesized $\text{IrO}_2\text{-P-CoCH}/\text{PCC}$ was examined by X-ray diffraction (XRD). The diffraction peaks at 10.1, 17.3, 26.5, 30.4, 34.2, 36.5, 39.4, and 47.1° correspond to the crystallographic facets of rhombohedral $\text{Co}(\text{CO}_3)_{0.5}(\text{OH})0.11\text{H}_2\text{O}$ (JCPDS No. 48-0083), matching well with the (100), (020), (220), (300), (040), (301), (231), and (340) planes, respectively. Meanwhile, some crystal planes for IrO_2 , such as (110), (101), and (200), are certified by the characteristic peaks occurring at 27.9, 34.2, and 39.4°, respectively. Notably, the diffraction peaks of $\text{IrO}_2\text{-P-CoCH}/\text{PCC}$ are similar to those of CoCH/PCC , indicating that the decorated IrO_2 does not significantly alter the crystal structure of CoCH/PCC . However, the peak intensities of $\text{IrO}_2\text{-P-CoCH}$ at 34.2 and 39.4° are significantly lower than those of CoCH , which might be attributed to the decreased amount of CoCH caused by the plasma etching, as well as to the influence of the adsorbed IrO_2 on the crystalline properties of CoCH . Furthermore, the chemical states of the elements on the surface of $\text{IrO}_2\text{-P-CoCH}$ are characterized by X-ray photoelectron spectroscopy (XPS). The detected elements include Co, Ir, O, and C (Figure S10a), with different elemental contents observed for $\text{IrO}_2\text{-P-CoCH}/\text{PCC}$ and $\text{IrO}_2\text{-CoCH}/\text{PCC}$ catalysts (Figure S11). Figure 3b shows the high-resolution Co 2p spectra for CoCH/PCC and $\text{IrO}_2\text{-P-CoCH}/\text{PCC}$, which reveal four distinct peaks. The peaks at 781.7 and 797.7 eV are assigned to $\text{Co} 2p_{3/2}$ and $\text{Co} 2p_{1/2}$, respectively, while the peaks at 787.5 and 803.9 eV correspond to satellite peaks.^{27,28} Compared with CoCH/PCC , the binding energies of $\text{Co} 2p_{3/2}$ (781.1 eV) and $\text{Co} 2p_{1/2}$ (797 eV) in $\text{IrO}_2\text{-P-CoCH}/\text{PCC}$ are shifted negatively by approximately 0.6 and 0.7 eV, respectively. This shift indicates that the coated IrO_2 effectively modifies the electronic structure around Co.^{29–31} For a detailed analysis of the valence states of Co, the Gaussian curve-fitting method is employed. As depicted in Figure 3b, two fitting peaks at 783.1

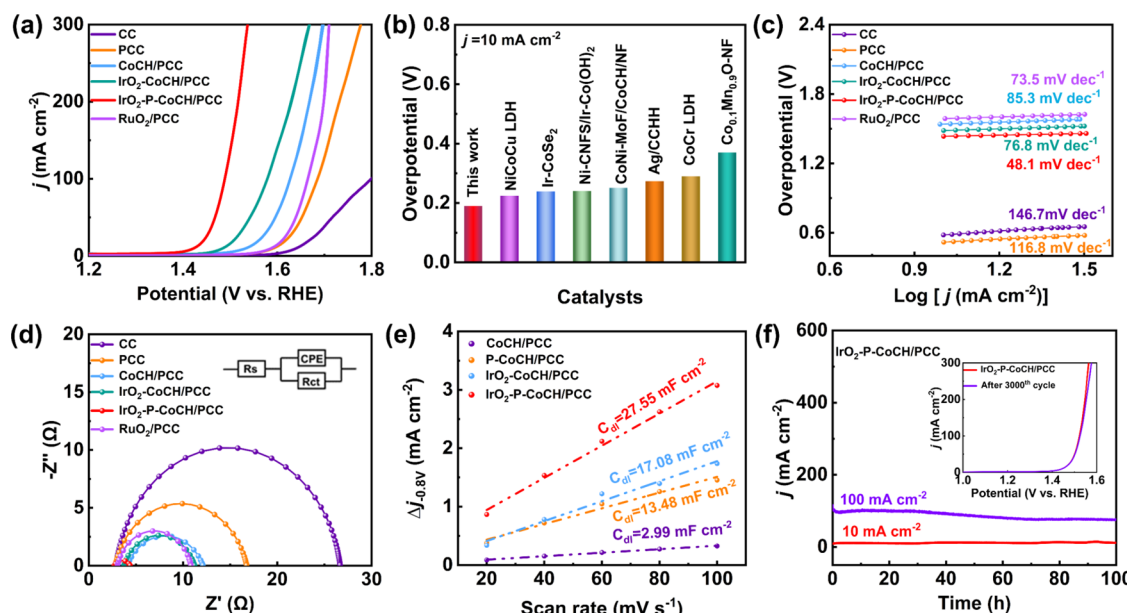


Figure 4. OER performance of different catalysts in 1.0 M KOH electrolyte. (a) Polarization curves, (b) comparison of the overpotential of $\text{IrO}_2\text{-P-CoCH/PCC}$ with other reported electrocatalysts at j_{10} , (c) Tafel slope, (d) Nyquist plots, (e) C_{dl} values derived from a linear fit to the relationship between capacitance current and scanning rate, and (f) $\text{IrO}_2\text{-P-CoCH/PCC}$ chrono-current curves recorded at j_{10} and j_{100} for 100 h and the polarization curves of $\text{IrO}_2\text{-P-CoCH/PCC}$ before and after 3000 cycles (inset).

eV ($\text{Co } 2p_{3/2}$) and 799.2 eV ($\text{Co } 2p_{1/2}$) are assigned to Co^{2+} , while those occurring at 780.8 eV ($\text{Co } 2p_{3/2}$) and 796.7 eV ($\text{Co } 2p_{1/2}$) are attributed to Co^{3+} . A notable enhancement in the intensity of the Co^{3+} peak is observed in $\text{IrO}_2\text{-P-CoCH/PCC}$ compared to pristine CoCH/PCC , indicating that the Co^{2+} is oxidized to a higher density of Co^{3+} on the catalyst surface by DBD plasma. Co^{3+} is widely regarded as the real active site in the OER process.^{30,32–34} To further investigate the electron interaction, the Ir 4f spectra are analyzed (Figure 3c), and the spin-orbit peaks at 62.6 and 65.5 eV can be assigned to $4f_{7/2}$ and $4f_{5/2}$ of Ir³⁺ which are the typical characteristic peaks of Ir^{3+} (peaks at 62.4 and 65.5 eV) and Ir^{4+} (peaks at 63.2 and 67.1 eV).^{37,38} This means that the value state of the decorated Ir is approximately +4, with most of the Ir remaining in the +3 valence state. Figure S10b shows the fitted C 1s spectrum, and it contains chemical states of C–C (284.7 eV), C=O (286.3 eV), and O=C–O (288.9 eV),³⁹ which indicates that the polar groups are grafted on the $\text{IrO}_2\text{-P-CoCH/PCC}$ surface under the function of DBD plasma. For the N 1s spectrum (Figure 3d), the peak near 399.9 eV is mainly attributed to the C–N bond,⁴⁰ and the newly formed peak at 401.8 eV for $\text{IrO}_2\text{-P-CoCH/PCC}$ is assigned to the N–O bond induced by the air–DBD plasma. Figure 3e exhibits the O 1s spectrum of $\text{IrO}_2\text{-P-CoCH/PCC}$, and it can be divided into three peaks at 530.3, 531.6, and 532.8 eV, which are well matched with metal–oxygen bonding, oxygen vacancy, and CO_3^{2-} , respectively.^{41,42} By comparing with the O 1s spectrum of bare CoCH/PCC , a distinctly increased peak intensity of oxygen vacancies and metal oxygen for $\text{IrO}_2\text{-P-CoCH/PCC}$ is observed (Figure S12 and Table S2).^{43,44} Electron paramagnetic resonance (EPR) is another effective strategy to detect the aqueous O_v . Figure 3f exhibits a symmetric peak at $g = 2.003$ for all electrocatalysts, indicating unpaired electrons in the O_v . Meanwhile, the EPR signal intensity of $\text{IrO}_2\text{-P-CoCH/PCC}$ is significantly stronger than that of $\text{IrO}_2\text{-CoCH/PCC}$, further verifying the existence of O_v sites,^{45,46} which manifests that the intermediate etched by

plasma can effectively increase the formation of oxygen vacancies. Therefore, the synergistic effect of heterointerface phases and the formed O_v are quite helpful for improving the electrocatalytic activity of $\text{IrO}_2\text{-P-CoCH/PCC}$, causing a high OER performance.

3.2. OER Characterization. The OER performance of the electrocatalysts was assessed in 1 M KOH using a three-electrode system. Figure 4a displays the linear sweep voltammetry (LSV) curves of $\text{IrO}_2\text{-P-CoCH/PCC}$, $\text{IrO}_2\text{-CoCH/PCC}$, CoCH/PCC , $\text{RuO}_2\text{/PCC}$, PCC , and CC samples with the iR correction. Remarkably, the $\text{IrO}_2\text{-P-CoCH/PCC}$ exhibits a superior OER electrocatalytic activity compared to the other tested samples. Note that the overpotentials of resulting $\text{IrO}_2\text{-P-CoCH/PCC}$ required to achieve current densities of j_{10} , j_{100} , and j_{300} are only 190, 250, and 300 mV, respectively, significantly lower than those of $\text{IrO}_2\text{-CoCH/PCC}$ (250 mV/ j_{10} , 340 mV/ j_{100} , and 430 mV/ j_{300}), CoCH/PCC (300 mV/ j_{10} , 390 mV/ j_{100} , and 460 mV/ j_{300}), PCC (360 mV/ j_{10} , 450 mV/ j_{100} , and 540 mV/ j_{300}), and CC (410 mV/ j_{10} , 560 mV/ j_{100}). Additionally, the overpotential of optimized $\text{IrO}_2\text{-P-CoCH/PCC}$ is notably lower than that of $\text{RuO}_2\text{/PCC}$ (Table S3). These results underscore the positive impact of a small amount of noble metal of IrO_2 and the assistance of DBD plasma for enhancing the OER activity of the catalyst. Furthermore, the OER activity of $\text{IrO}_2\text{-P-CoCH/PCC}$ is also very competitive to those reported high-quality electrocatalysts (Figure 4b) stimulated with j_{10} , such as NiCoCu LDH (224 mV),⁴⁷ $\text{Ni-CNFS/Ir-Co(OH)}_2$ (240 mV),³⁸ Ir-CoSe_2 (239 mV),⁴⁸ CoNi-MoF/CoCH/NF (251 mV),⁴⁹ CoCr LDH (290 mV),⁵⁰ $\text{Co}_{0.1}\text{Mn}_{0.9}\text{O-NF}$ (370 mV),⁵¹ V-CoCH (183 mV),³² and some other engineered catalytic materials (Table S4).

Meanwhile, to explore the reactive mechanisms of the resulting samples, the Tafel slopes (Figure 4c) are calculated according to the obtained LSV curves. The Tafel value of $\text{IrO}_2\text{-P-CoCH/PCC}$ is about 48.1 mV dec⁻¹, which is smaller than those of $\text{IrO}_2\text{-CoCH/PCC}$ (76.80 mV dec⁻¹), CoCH/PCC

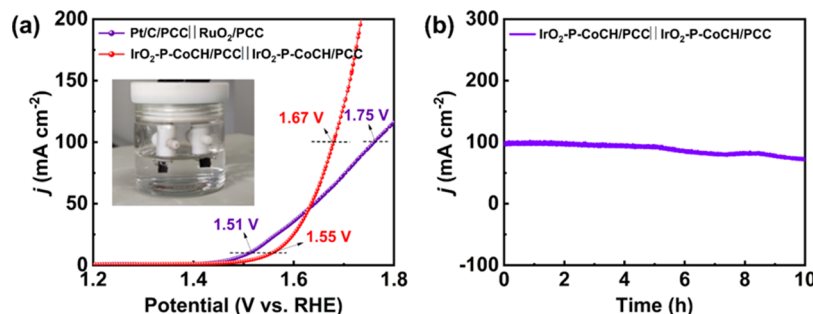


Figure 5. (a) Polarization curves achieved by two-electrode cells of IrO₂-P-CoCH/PCC||IrO₂-P-CoCH/PCC and Pt/C/PCC||RuO₂/PCC and (b) long-term stability of two-electrode cell of IrO₂-P-CoCH/PCC pushed with j_{100} .

(85.25 mV dec⁻¹), PCC (116.83 mV dec⁻¹), and CC (146.71 mV dec⁻¹), including the noble catalyst of RuO₂/PCC (73.48 mV dec⁻¹). This result indicates that the IrO₂-P-CoCH/PCC exhibits fast reactive kinetics in the OER process. Mass activity (MA) is also an important indicator for judging the catalytic activity of materials. As can be seen in Figure S13a and Table S5, the MA of IrO₂-P-CoCH/PCC pushed with an overpotential of 300 mV is about 30.12 A g^{-1} , which is much higher than those of IrO₂-CoCH/PCC (6.37 A g^{-1}), CoCH/PCC (1.69 A g^{-1}), and RuO₂/PCC (1.12 A g^{-1}). To further explore the kinetics of electrocatalytic reactions, the electrochemical impedance spectroscopy (EIS) measurements are performed (Figure 4d), and the Nyquist plots show that the semicircle of IrO₂-P-CoCH/PCC (R_{ct}) is only 1.7 Ω , which is far smaller than those of IrO₂-CoCH/PCC (7.5 Ω), CoCH/PCC (8.0 Ω), PCC (13.95 Ω), CC (23.76), and RuO₂/PCC (7.8 Ω). Therefore, the nearly metallic property of the IrO₂-P-CoCH/PCC electrode can transfer the electron to the water molecule at a faster speed, causing a higher efficiency for O₂ generation. Normally, the values of electrochemical double-layer capacitance C_{dl} and ECSA (C_{dl}/C_s , $C_s = 0.04 \text{ mF cm}^{-2}$) are also used to manifest the electrocatalytic activity.⁵² As shown in Figure 4e, the calculated values of $C_{\text{dl}}/\text{ECSA}$ of IrO₂-P-CoCH/PCC (27.55 $\text{mF cm}^{-2}/688.75 \text{ cm}^{-2}$) are much higher than those of IrO₂-CoCH/PCC (17.08 $\text{mF cm}^{-2}/427 \text{ cm}^{-2}$), P-CoCH/PCC (13.48 $\text{mF cm}^{-2}/337 \text{ cm}^{-2}$), and CoCH/PCC (2.99 $\text{mF cm}^{-2}/74.75 \text{ cm}^{-2}$) samples. At the same time, the IrO₂-P-CoCH/PCC only requires 145 mV to induce a normalized 0.01 mA cm^{-2} ECSA (Figure S13b). These results suggest that the modification of DBD plasma and IrO₂-decorated greatly increases the surface active sites of the IrO₂-P-CoCH/PCC electrode. Certainly, the surface roughness of IrO₂-P-CoCH nanocone is improved greatly under the function of DBD plasma, which obviously increases the contact area between the catalyst surface exposure to the electrolytic medium, thus causing an excellent OER catalyst based on carbon fiber. Except for the OER activity, the stability of the catalyst is also a critical factor for determining the electrocatalytic performance of the electrode material. In this work, the electrocatalytic stability and durability of IrO₂-P-CoCH/PCC are, respectively, indicated by the long-term cyclic voltammetry and current-time ($I-t$) measurements. Figure 4f shows the sustainability of the IrO₂-P-CoCH/PCC catalyst stimulated with different constant current densities in 1 M KOH. It is noteworthy that the $I-t$ curve remains very stable at j_{100} , and the decaying step is only 1.3% over 100 h. Meanwhile, the long-term stability of IrO₂-P-CoCH/PCC under a high current density (j_{100}) for 100 h is also achieved. Besides, the excellent electrochemical stability of the IrO₂-P-CoCH/PCC

catalyst is further confirmed by the nearly overlapped LSV curves before and after 3000 cycles (inset of Figure 4f).

Furthermore, the high OER activity of IrO₂-P-CoCH/PCC is also indicated by the high efficiency for O₂ generation, and the oxygen production of IrO₂-P-CoCH/PCC in 1 M KOH is measured by using a conventional drainage method. As shown in Figure S13c, the O₂ production of IrO₂-P-CoCH/PCC pushed with j_{10} is about 0.95 mmol h^{-1} , which is better than the recently reported high-performance catalysts, such as N-NiMoO₄/NiS₂ (0.8 mmol h^{-1}),⁵³ Cu₃Se₂@CoSe₂-NiSe₂/PNCF (0.90 mmol h^{-1}),⁵⁴ W-NiS_{0.5}Se_{0.5}/NF (0.89 mmol h^{-1}),⁵⁵ and Co(OH)₂/Ag/FeP/Ti (0.50 mmol h^{-1}).⁵⁶ Note that the optimized IrO₂-P-CoCH/PCC also exhibits high HER activity in the alkaline medium. Figure S14a displays the LSV curves of the CC, PCC, CoCH/PCC, IrO₂-CoCH/PCC, IrO₂-P-CoCH/PCC, and Pt/C/PCC catalysts after an iR correction in 1 M KOH. The overpotentials for driving j_{10} , j_{100} , and j_{300} are only 95, 253, and 331 mV, respectively. Meanwhile, the Tafel slope of IrO₂-P-CoCH/PCC (Figure S14b) is only 119.5 mV dec⁻¹, which is much smaller than those of CC (189.1 mV dec⁻¹), PCC (160.8 mV dec⁻¹), CoCH/PCC (136.3 mV dec⁻¹), IrO₂-CoCH/PCC (125.4 mV dec⁻¹), and Pt/C/PCC (160.8 mV dec⁻¹), indicating that a fast reactive kinetics occurs in the HER process. Figure S14c shows the detected interface charge transfer resistances (R_{ct}) of IrO₂-P-CoCH/PCC, and the low R_{ct} value (8.2 Ω) of the catalyst also manifests that the reactive species can be quickly transferred between the electrodes and electrolyte in the HER process.

Based on the excellent OER and HER activity of the optimized catalyst, a two-electrode cell of IrO₂-P-CoCH/PCC||IrO₂-P-CoCH/PCC is assembled for estimating the performance of overall water splitting. As shown in Figure 5a, it can be seen that the potentials for generating current densities of j_{10} and j_{100} are about 1.55 and 1.67 V, which are even better than those of cells assembled by the Pt/C/PCC||RuO₂/PCC electrodes (1.51 V/ j_{10} and 1.75 V/ j_{100}) as well as lower than most recently reported high-quality catalysts (Table S6). At the same time, we also tested the electrocatalytic stability of the IrO₂-P-CoCH/PCC||IrO₂-P-CoCH/PCC electrode at a current density of j_{100} , and the result suggests that IrO₂-P-CoCH/PCC presents an excellent bifunctional activity and stability in an alkaline medium (Figure 5b).

3.3. Reaction Mechanism Analysis. For explaining the catalytic mechanism of IrO₂-P-CoCH/PCC, density functional theory (DFT) calculations are carried out to reveal the catalytic activity underpinned by different heterointerfaces between IrO₂ and CoCH. The (300) plane of CoCH and the (101) plane of IrO₂ are employed as a theoretical model (Figure 6a) because the HRTEM image shows that the (300)

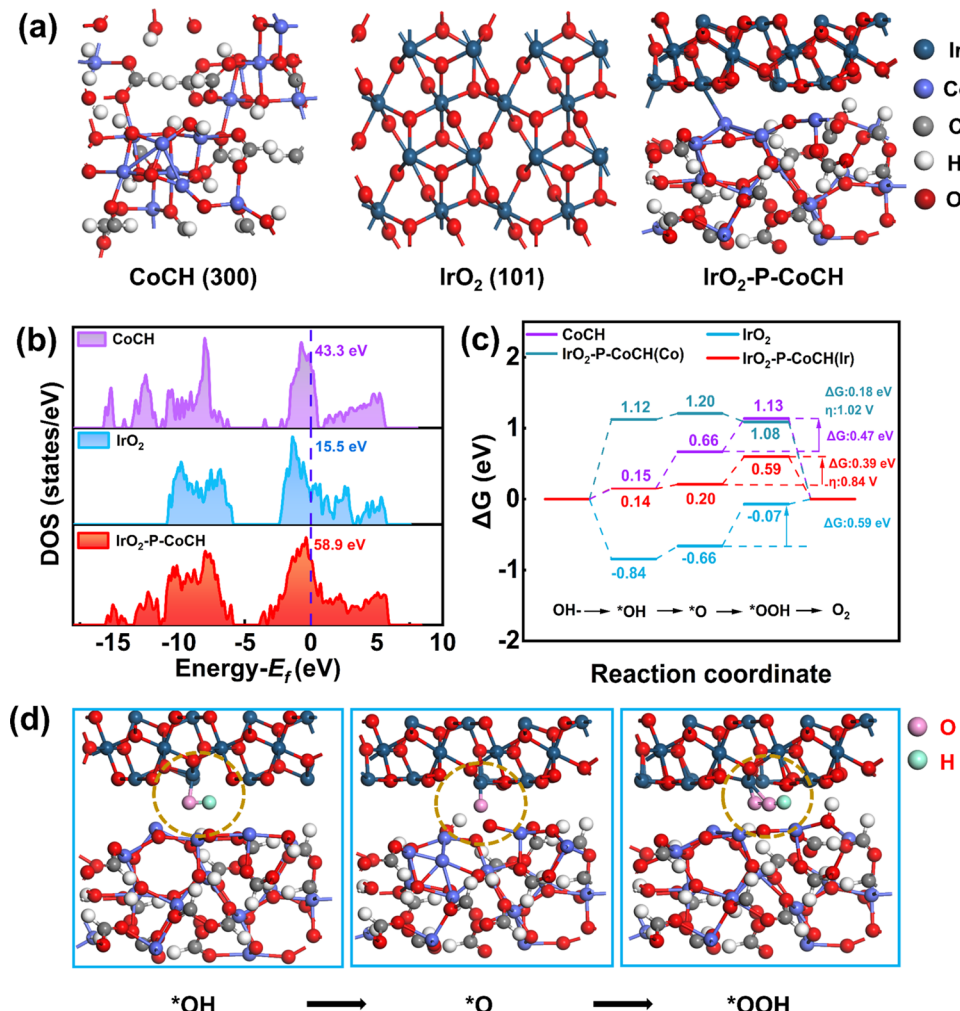


Figure 6. Theoretical insights into the catalyst OER performance by DFT calculations. (a) Atomistic models, (b) electron densities of states (DOS), (c) Gibbs free energies, and (d) optimized intermediates during the OER process on the IrO₂-P-CoCH/PCC surface.

and (101) planes are the primary exposed planes on the catalyst surface for forming interfaces. Figure 6b shows the density of states (DOS) diagram, and it can be seen that the electronic states of CoCH (43.3 eV), IrO₂ (15.5 eV), and IrO₂-P-CoCH (58.9 eV) all cross the Fermi level, indicating their metallic properties. Especially, the electronic DOS of the IrO₂-P-CoCH phase is far higher around E_f than those of CoCH and IrO₂, and the formation of the Ir site on IrO₂-P-CoCH widens the d-band as well as the shifted d-band center to the Fermi level. Note that the highest DOS of the Ir site in IrO₂-P-CoCH stimulated by the increased electron density of the Co 3d orbital will benefit the formation of OOH* species.⁵⁷ Therefore, the higher position of the d-band center of IrO₂-P-CoCH (Ir) effectively increases the adsorption capability of intermediate species and facilitates intermediate desorption. In addition, the formation of a heterogeneous interface between CoCH and IrO₂ generates the synergistic effect, eventually causing a high electrocatalytic activity of IrO₂-P-CoCH for water splitting.

As demonstrated in Figure 6c,6d, the OER process of IrO₂-P-CoCH has four elementary steps, which involve the $^*\text{OH}$, $^*\text{O}$, and $^*\text{OOH}$ intermediate species. The generation of the $^*\text{OOH}$ intermediate on the CoCH surface from the $^*\text{O}$ adsorbed intermediate is the rate-determining step (RDS)⁵⁸ for the OER process because of the higher reaction energy

barrier (0.47 eV). After the incorporation of IrO₂ onto the CoCH surface, the OER RDS of IrO₂-P-CoCH is still the reactive step from $^*\text{O}$ to $^*\text{OOH}$, except a lower reaction energy barrier (0.39 eV) is needed. Noticeably, the DFT results exhibit that the free energies of oxidative transition ($M^*\text{O}$, $\Delta_{\text{G}^*\text{OOH}-\Delta_{\text{G}^*\text{O}}}$) for IrO₂-P-CoCH, IrO₂, and CoCH are all larger than those of the adsorption process of OH⁻, the deprotonation of M^{*}OH ($\Delta_{\text{G}^*\text{O}-\Delta_{\text{G}^*\text{OH}}}$), and the oxygen release process, which is consistent with the results of Tafel values. As can be seen from Figure S15, the highest barrier energies for CoCH (300) and IrO₂ (101) are 0.47 and 0.59 eV, respectively. Therefore, compared with IrO₂ (101), the CoCH (300) can improve the adsorption of reactive intermediates and accelerate the reactive rate of oxygen generation. On the other hand, the effect of Ir or Co sites in IrO₂-P-CoCH on the OER activity is also investigated. Under an applied potential of 1.23 V, the rate-determining step is still $^*\text{OOH}$ production, and the overpotential of the Co site in IrO₂-P-CoCH is significantly higher than that of the Ir site. Therefore, the Ir site of IrO₂-P-CoCH is the active center, which is very beneficial for the OER. It should be noted that each step of the OER that occurred on the CoCH surface is well regulated by the decorated IrO₂, and all the energy barriers of the formed heterostructures are far lower than those of single-phase

materials, indicating that the IrO_2 introduction is vital to promote the OER activity of the engineered electrocatalyst.

3.4. Enhancement Mechanism of Electrochemical Activity. According to the results mentioned above, the possible factors causing an excellent electrocatalytic activity of engineered $\text{IrO}_2\text{-P-CoCH/PCC}$ are as follows:

- (i) Under the function of air-DBD plasma, the binding strength between the carbon fiber and CoCH is significantly improved, which significantly improves the electrocatalytic stability of the catalyst. Note that the $I-t$ curves pushed with j_{100} (Figure S16) further verify that the electrocatalytic stability of $\text{IrO}_2\text{-P-CoCH/PCC}$ is far stable than that of $\text{IrO}_2\text{-CoCH/CC}$.
- (ii) The calculated CV curves are shown in Figure S17, and the C_{dl} value of the $\text{IrO}_2\text{-P-CoCH/PCC}$ samples, as shown in Figure S17, is about 27.55 mF cm^{-2} , which is much higher than those of $\text{IrO}_2\text{-CoCH/PCC}$ (17.08 mF cm^{-2}), P-CoCH/PCC (13.48 mF cm^{-2}), and CoCH/PCC (2.99 mF cm^{-2}). Meanwhile, because the catalyst surface is covered with many tiny bumps, the larger contact area of $\text{IrO}_2\text{-P-CoCH/PCC}$ is very positive for increasing the catalytic performance. Note that the specific surface area of CoCH/PCC can significantly increase when it is treated by DBD plasma, and the exposed active sites are much easier to absorb the Ir ions, causing a higher OER or HER activity. In addition, the formed oxygen vacancies etched by DBD plasma also increase the OER or HER performance greatly.
- (iii) The lower electrochemical impedance of $\text{IrO}_2\text{-P-CoCH/PCC}$ (1.7Ω) in the OER process indicates the near-metal characteristics of the engineered catalyst, which enhances the electrocatalytic efficiency, causing a high output of oxygen gas with a low current density.
- (iv) According to the results of DFT simulations, the synergistic effect between the IrO_2 and CoCH phases significantly reduces the corresponding adsorption free energy (ΔG_{ad}) values, as well as providing abundant active centers for lowering the energy barriers and increasing the electron transfer rate, thereby causing faster electrolysis kinetics in the OER process.

4. CONCLUSIONS

In conclusion, the $\text{IrO}_2\text{-P-CoCH/PCC}$ catalyst is successfully synthesized on a carbon-based material using a simple hydrothermal and plasma modification method. Through two-step modifications involving air-DBD plasma, the active sites on both carbon cloth and CoCH surfaces are effectively created, facilitating a subsequent hydrothermal reaction and IrO_2 decoration. The resulting micrometer-scale water-lotus-like flowers, coupled with the rough concave–convex shape of the catalyst surface, provide a large reactive area and abundant active sites, as well as etched rich oxygen vacancies. Consequently, the engineered $\text{IrO}_2\text{-P-CoCH/PCC}$ exhibits excellent electrocatalytic activity and stability in alkaline conditions, and the overpotentials stimulated with current densities of j_{10} , j_{100} , and j_{300} are only 190, 250, and 300 mV in the OER process, surpassing the benchmarked catalysts of RuO_2 . Furthermore, even after 100 h at j_{10} , the current density only decreases by 1.3%, demonstrating outstanding electrochemical stability of carbon fiber-based $\text{IrO}_2\text{-P-CoCH}$. Additionally, an alkaline electrolyzer assembled with $\text{IrO}_2\text{-P-CoCH/PCC}$ catalysts can achieve a current density of 10

mA cm^{-2} at a tank voltage of 1.55 V, outperforming the system integrated with commercial Pt/C and RuO_2 electrodes. Based on the theory results, the formed heterointerface between IrO_2 and CoCH phases has a larger electron state density and lower ΔG_{ad} values near the Fermi energy level, thus demonstrating superior OER activity. This work presents a novel approach for engineering high-performance OER electrocatalysts on soft electrode substrates, expanding the option range for designing transition metal electrocatalysts decorated by noble metals.

■ ASSOCIATED CONTENT

SI Supporting Information

The Supporting Information is available free of charge at <https://pubs.acs.org/doi/10.1021/acs.inorgchem.4c02591>.

The physio-chemical characteristics of materials, such as the effects of DBD plasma and fabricating conditions on the catalytic activity of catalysts; SEM images; XRD patterns; TEM image; EDS spectrum; XPS spectra; cyclic voltammetry curves; chronopotentiometry curve; tables (PDF).

■ AUTHOR INFORMATION

Corresponding Author

Guangliang Chen – Huzhou Key Laboratory of Environmental Functional Materials and Pollution Control, Huzhou University, Huzhou 313000, P. R. China;
ORCID: [0000-0002-8556-1741](https://orcid.org/0000-0002-8556-1741); Email: glchen@zjhu.edu.cn

Authors

Ying Xie – Key Laboratory for Rare Earth Chemistry and Application of Liaoning Province, College of Science, Shenyang University of Chemical Technology, Shenyang 110000 Liaoning, P. R. China

Jinfeng Qiu – Key Laboratory for Rare Earth Chemistry and Application of Liaoning Province, College of Science, Shenyang University of Chemical Technology, Shenyang 110000 Liaoning, P. R. China; Huzhou Key Laboratory of Environmental Functional Materials and Pollution Control, Huzhou University, Huzhou 313000, P. R. China

Yingchun Guo – Huzhou Key Laboratory of Environmental Functional Materials and Pollution Control, Huzhou University, Huzhou 313000, P. R. China

Peisong Tang – Huzhou Key Laboratory of Environmental Functional Materials and Pollution Control, Huzhou University, Huzhou 313000, P. R. China

Bin He – Huzhou Key Laboratory of Environmental Functional Materials and Pollution Control, Huzhou University, Huzhou 313000, P. R. China

Complete contact information is available at:

<https://pubs.acs.org/10.1021/acs.inorgchem.4c02591>

Notes

The authors declare no competing financial interest.

Safety Statement: High voltage for generating DBD plasma is very dangerous, and no uncommon chemical hazards are noted.

■ ACKNOWLEDGMENTS

This work received financial support from the National Natural Science Foundation of China (Nos. 52177162 and 22308080), the Natural Science Foundations of Zhejiang province (Nos.

LZ22E070003 and LQ24E040002), the Natural Science Foundation of Huzhou City (No. 2023YZ18), and China Scholarship Council (No. 202208210230).

■ REFERENCES

- (1) Wang, Y.; Chen, G.; Li, T. One-Step Engineering Co_8FeS_8 Electrocatalyst Based on Co-Fe Bimetal Foam for a Highly-Efficient Oxygen Evolution Reaction. *Int. J. Hydrogen Energy* **2024**, *53*, 613–621.
- (2) Liu, X.; Huang, J.; Li, T.; Chen, W.; Chen, G.; Han, L.; Ostrikov, K. K. High-Efficiency Oxygen Evolution Catalyzed by Sn-Co-Ni Phosphide with Oriented Crystal Phases. *J. Mater. Chem. A* **2022**, *10* (25), 13448–13455.
- (3) Yu, Z. Y.; Duan, Y.; Feng, X. Y.; Yu, X.; Gao, M. R.; Yu, S. H. Clean and Affordable Hydrogen Fuel from Alkaline Water Splitting: Past, Recent Progress, and Future Prospects. *Adv. Mater.* **2021**, *33* (31), No. 2007100.
- (4) Ma, S.; Huang, J.; Zhang, C.; Chen, G.; Chen, W.; Shao, T.; Li, T.; Zhang, X.; Gong, T.; Ostrikov, K. K. One-Step In-Situ Sprouting High-Performance $\text{NiCoS}_x\text{Se}_y$ Bifunctional Catalysts for Water Electrolysis at Low Cell Voltages and High Current Densities. *Chem. Eng. J.* **2022**, *435*, No. 134859.
- (5) Chen, W.; Zhang, Y.; Chen, G.; Huang, R.; Wu, Y.; Zhou, Y.; Hu, Y.; Ostrikov, K. K. Hierarchical Porous Bimetal-Sulfide Bi-Functional Nanocatalysts for Hydrogen Production by Overall Water Electrolysis. *J. Colloid Interface Sci.* **2020**, *560*, 426–435.
- (6) Zhang, Q.; Chen, W.; Chen, G.; Huang, J.; Song, C.; Chu, S.; Zhang, R.; Wang, G.; Li, C.; Ostrikov, K. K. Bi-Metallic Nitroxide Nanodot-Decorated Tri-Metallic Sulphide Nanosheets by On-Electrode Plasma-Hydrothermal Sprouting for Overall Water Splitting. *Appl. Catal., B* **2020**, *261*, No. 118254.
- (7) Zuo, Y.; Bellani, S.; Saleh, G.; Ferri, M.; Shinde, D. V.; Zappia, M. I.; Buha, J.; Brescia, R.; Prato, M.; Pascazio, R.; et al. Ru-Cu Nanoheterostructures for Efficient Hydrogen Evolution Reaction in Alkaline Water Electrolyzers. *J. Am. Chem. Soc.* **2023**, *145* (39), 21419–21431.
- (8) Chen, S.; Wang, S.; Hao, P.; Li, M.; Zhang, Y.; Guo, J.; Ding, W.; Liu, M.; Wang, J.; Guo, X. N. O-C Nanocage-Mediated High-Efficient Hydrogen Evolution Reaction on IrNi@N,O-C Electrocatalyst. *Appl. Catal., B* **2022**, *304*, No. 120996.
- (9) Kim, M.; Park, J.; Wang, M.; Wang, Q.; Kim, M. J.; Kim, J. Y.; Cho, H.-S.; Kim, C.-H.; Feng, Z.; Kim, B.-H.; Lee, S. W. Role of Surface Steps in Activation of Surface Oxygen Sites on Ir Nanocrystals for Oxygen Evolution Reaction in Acidic Media. *Appl. Catal., B* **2022**, *302*, No. 120834.
- (10) Wang, H.; Chen, J.; Lin, Y.; Wang, X.; Li, J.; Li, Y.; Gao, L.; Zhang, L.; Chao, D.; Xiao, X.; Lee, J. Electronic Modulation of Non-van der Waals 2D Electrocatalysts for Efficient Energy Conversion. *Adv. Mater.* **2021**, *33* (26), No. 2008422.
- (11) Li, W.; Li, M.; Wang, C.; Lu, X. Iridium-Incorporated Cobalt Nanofibers as Efficient and Robust Bifunctional Catalysts for High-Performance Water Electrolysis. *Sci. China Mater.* **2023**, *66* (3), 1024–1032.
- (12) Liu, J.; Xiao, J.; Wang, Z.; Yuan, H.; Lu, Z.; Luo, B.; Tian, E.; Waterhouse, G. I. Structural and Electronic Engineering of Ir-Doped Ni-(oxy)hydroxide Nanosheets for Enhanced Oxygen Evolution Activity. *ACS Catal.* **2021**, *11* (9), 5386–5395.
- (13) Wen, T.; Liu, W.; Wang, L.; Gong, Y. Controlled Synthesis of Fe-Ni-S@CoSe_2 on Nickel Foam as an Efficient Electrocatalyst for Oxygen Evolution Reaction. *J. Alloys Compd.* **2023**, *966*, No. 171550.
- (14) Li, T.; Zhang, J.; Ren, R.; Tian, Y. Atomic-Scale Insights into Single-Atom Embedded on N-Doped Carbon Electrocatalyst Mechanisms for Sulfur Reduction Reaction in LiS Batteries. *J. Energy Storage* **2024**, *88*, No. 111600.
- (15) Liu, S.; Hui, K.; Hui, K.; Jadhav, V. V.; Xia, Q. X.; Yun, J. M.; Cho, Y.; Mane, R. S.; Kim, K. H. Facile Synthesis of Microsphere Copper Cobalt Carbonate Hydroxides Electrode for Asymmetric Supercapacitor. *Electrochim. Acta* **2016**, *188*, 898–908.
- (16) Jiang, B.; Liu, W.; Ren, Z.; Guo, R.; Huang, Y.; Xu, C.; Kang, F. Oxygen Plasma Modified Carbon Cloth with $\text{C}=\text{O}$ Zincophilic Sites as a Stable Host for Zinc Metal Anodes. *Front. Chem.* **2022**, *10*, No. 899810.
- (17) Zai, S. F.; Zhou, Y. T.; Yang, C. C.; Jiang, Q. Al, Fe-codoped CoP Nanoparticles Anchored on Reduced Graphene Oxide as Bifunctional Catalysts to Enhance Overall Water Splitting. *Chem. Eng. J.* **2021**, *421*, No. 127856.
- (18) Wang, L.; Yu, H.; Zhao, S.; Ma, H.; Li, L.; Hu, F.; Li, L.; Pan, H.; El-Khatib, K.; Peng, S. Electronic Modulation of Cobalt-Molybdenum Oxide via Te Doping Embedded in a Carbon Matrix for Superior Overall Water Splitting. *Inorg. Chem. Front.* **2022**, *9* (15), 3788–3796.
- (19) Karmakar, A.; Srivastava, S. K. Hierarchically Hollow Interconnected Rings of Nickel Substituted Cobalt Carbonate Hydroxide Hydrate as Promising Oxygen Evolution Electrocatalyst. *Int. J. Hydrogen Energy* **2022**, *47* (53), 22430–22441.
- (20) Chen, G.; Xiang, H.; Guo, Y.; Huang, J.; Chen, W.; Chen, Z.; Li, T.; Ostrikov, K. Yttrium-and Nitrogen-Doped NiCo Phosphide Nanosheets for High-Efficiency Water Electrolysis. *Carbon Energy* **2024**, No. e522.
- (21) Kresse, G.; Joubert, D. From Ultrasoft Pseudopotentials to the Projector Augmented-Wave Method. *Phys. Rev. B* **1999**, *59*, 1758.
- (22) Perdew, J. P.; Burke, K.; Ernzerhof, M. Generalized Gradient Approximation Made Simple. *Phys. Rev. Lett.* **1996**, *77*, 3865–3868.
- (23) Grimme, S.; Antony, J.; Ehrlich, S.; Krieg, H. A Consistent and Accurate Ab initio Parametrization of Density Functional Dispersion Correction (DFT-D) for the 94 Elements H-Pu. *J. Chem. Phys.* **2010**, *132*, No. 154104.
- (24) Li, T. T.; Yu, Y. F.; Pei, M. Y. Dual-Atom Doping Carbon Materials as Highly Efficient Electrocatalysts for Lithium–Sulfur Batteries: Bimetallic Cooperation Mechanism. *J. Phys. Chem. C* **2023**, *127*, 6271–6279.
- (25) Chen, D.; Xu, Z.; Chen, W.; Chen, G.; Huang, J.; Song, C.; Zheng, K.; Zhang, Z.; Hu, X.; Choi, H. S.; Ostrikov, K. K. Mulberry-Inspired Nickel-Niobium Phosphide on Plasma-Defect-Engineered Carbon Support for High-Performance Hydrogen Evolution. *Small* **2020**, *16* (43), No. 2004843.
- (26) Liu, Z.; Zhao, Z.; Wang, Y.; Dou, S.; Yan, D.; Liu, D.; Xia, Z.; Wang, S. In Situ Exfoliated, Edge-Rich, Oxygen-Functionalized Graphene from Carbon Fibers for Oxygen Electrocatalysis. *Adv. Mater.* **2017**, *29* (18), No. 1606207.
- (27) Li, H.; Wang, J.; Tjardts, T.; Barg, I.; Qiu, H.; Müller, M.; Krahmer, J.; Askari, S.; Veziroglu, S.; Aktas, C.; et al. Plasma-Engineering of Oxygen Vacancies on NiCo_2O_4 Nanowires with Enhanced Bifunctional Electrocatalytic Performance for Rechargeable Zinc-air Battery. *Small* **2024**, *20* (24), No. 2310660.
- (28) Li, Y.; Du, Q.-X.; Cui, J.; Yang, H.-W.; Qian, H. Heterostructure $\text{CoS}_2/\text{MoS}_2$ Nanosheets as a Dual-Active Electrocatalyst for the Oxygen Evolution Reaction. *Inorg. Chem.* **2024**, *63* (4), 1954–1961.
- (29) Wang, P.; Zhang, L.; Wang, Z.; Bu, D.; Zhan, K.; Yan, Y.; Yang, J.; Zhao, B. N and Mn Dual-Doped Cactus-Like Cobalt Oxide Nanoarchitecture Derived from Cobalt Carbonate Hydroxide as Efficient Electrocatalysts for Oxygen Evolution Reactions. *J. Colloid Interface Sci.* **2021**, *597*, 361–369.
- (30) Zhang, S.; Huang, B.; Wang, L.; Zhang, X.; Zhu, H.; Zhu, X.; Li, J.; Guo, S.; Wang, E. Boosted Oxygen Evolution Reactivity via Atomic Iron Doping in Cobalt Carbonate Hydroxide Hydrate. *ACS Appl. Mater. Interfaces* **2020**, *12* (36), 40220–40228.
- (31) Liu, X. Y.; Bi, H.; Li, L.; Li, B.; Wang, Y. H.; Shi, J.; Nie, J.; Huang, G. F.; Hu, W.; Huang, W. Q. Doping-Induced Facet Transformation Boosts Water Oxidation Activity of Cobalt Carbonate Hydroxide Hydrate. *Appl. Phys. Lett.* **2023**, *123* (9), No. 090501.
- (32) Ma, Z.; Ma, X.; Luo, W.; Jiang, Y.; Shen, W.; He, R.; Li, M. Dopant-Induced Surface Self-Etching of Cobalt Carbonate Hydroxide Boosts Efficient Water Splitting. *ChemSusChem* **2023**, *16* (7), No. e202201892.

- (33) Li, S.; Wang, H.; Ma, Z.; Xiao, Q.; Gao, Q.; Jiang, Y.; Shen, W.; He, R.; Li, M. Rapid Surface Reconstruction of Amorphous Co(OH)_x/WO_x with Rich Oxygen Vacancies to Promote Oxygen Evolution. *ChemSusChem* **2021**, *14* (24), 5534–5540.
- (34) Gao, L.; Cui, X.; Sewell, C. D.; Li, J.; Lin, Z. Recent Advances in Activating Surface Reconstruction for the High-Efficiency Oxygen Evolution Reaction. *Chem. Soc. Rev.* **2021**, *50* (15), 8428–8469.
- (35) Kang, J.; Fan, Q.; Zhou, W.; Zhang, Q.; He, S.; Yue, L.; Tang, Y.; Nguyen, L.; Yu, X.; You, Y.; et al. Iridium Boosts the Selectivity and Stability of Cobalt Catalysts for Syngas to Liquid Fuels. *Chem* **2022**, *8* (4), 1050–1066.
- (36) Casalongue, H. G. S.; Ng, M. L.; Kaya, S.; Friebel, D.; Ogasawara, H.; Nilsson, A. In Situ Observation of Surface Species on Iridium Oxide Nanoparticles During the Oxygen Evolution Reaction. *Angew. Chem., Int. Ed.* **2014**, *53* (28), 7169–7172.
- (37) He, Q.; Qiao, S.; Zhou, Q.; Zhou, Y.; Shou, H.; Zhang, P.; Xu, W.; Liu, D.; Chen, S.; Wu, X.; Song, L. Confining High-Valence Iridium Single Sites onto Nickel Oxyhydroxide for Robust Oxygen Evolution. *Nano Lett.* **2022**, *22* (9), 3832–3839.
- (38) Xu, J.; Cao, S.; Zhong, M.; Chen, X.; Li, W.; Yan, S.; Wang, C.; Wang, Z.; Lu, X.; Lu, X. Iridium Incorporated Cobalt-Based Hydroxide on Nickel-Contained Carbon Nanofibers Renders Highly Efficient Oxygen Evolution Reaction. *Sep. Purif. Technol.* **2023**, *324*, No. 124638.
- (39) Li, X.; Tang, Y.; Zhu, J.; Lv, H.; Zhao, L.; Wang, W.; Zhi, C.; Li, H. Boosting the Cycling Stability of Aqueous Flexible Zn Batteries via F Doping in Nickel–Cobalt Carbonate Hydroxide Cathode. *Small* **2020**, *16* (31), No. 2001935.
- (40) Yuan, C. Z.; Jiang, Y. F.; Wang, Z.; Xie, X.; Yang, Z. K.; Yousaf, A. B.; Xu, A. W. Cobalt Phosphate Nanoparticles Decorated with Nitrogen-Doped Carbon Layers as Highly Active and Stable Electrocatalysts for the Oxygen Evolution Reaction. *J. Mater. Chem. A* **2016**, *4* (21), 8155–8160.
- (41) Xu, L.; Jiang, Q.; Xiao, Z.; Li, X.; Huo, J.; Wang, S.; Dai, L. Plasma-Engraved Co₃O₄ Nanosheets with Oxygen Vacancies and High Surface Area for the Oxygen Evolution Reaction. *Angew. Chem.* **2016**, *128* (17), 5363–5367.
- (42) Tu, J.; Chen, X.; Xiong, X.; Chen, Y.; Ma, J.; Cao, H.; Li, A. Microwave Hydrothermal Electrodeposition of Nickel Carbonate Hydroxide/Cobalt hydroxide Film on Nickel Foam for Cement-Based Structural Supercapacitors. *Mater. Today Chem.* **2023**, *28*, No. 101365.
- (43) Su, R.; Gao, Y.; Chen, L.; Chen, Y.; Li, N.; Liu, W.; Gao, B.; Li, Q. Utilizing the Oxygen-Atom Trapping Effect of Co₃O₄ with Oxygen Vacancies to Promote Chlorite Activation for Water Decontamination. *Proc. Natl. Acad. Sci. U.S.A.* **2024**, *121* (11), No. e2319427121.
- (44) Zhong, D.; Li, T.; Wang, D.; Li, L.; Wang, J.; Hao, G.; Liu, G.; Zhao, Q.; Li, J. Strengthen Metal–Oxygen Covalency of CoFe-Layered Double Hydroxide for Efficient Mild Oxygen Evolution. *Nano Res.* **2022**, *15* (1), 162–169.
- (45) Liu, X.; Wei, S.; Cao, S.; Zhang, Y.; Xue, W.; Wang, Y.; Liu, G.; Li, J. Lattice Strain with Stabilized Oxygen Vacancies Boosts Ceria for Robust Alkaline Hydrogen Evolution Outperforming Benchmark Pt. *Adv. Mater.* **2024**, No. 2405970.
- (46) Gan, Y.; Ye, Y.; Dai, X.; Yin, X.; Cao, Y.; Cai, R.; Feng, B.; Wang, Q.; Wu, Y.; Zhang, X. Nickel Molybdate/Cobalt Iron Carbonate Hydroxide Heterojunction with Oxygen Vacancy Enables Interfacial Synergism to Trigger Oxygen Evolution Reaction. *J. Colloid Interface Sci.* **2024**, *658*, 343–353.
- (47) Raja, A.; Son, N.; Kim, Y.-I.; Kang, M. Hybrid Ternary NiCoCu Layered Double Hydroxide Electrocatalyst for Alkaline Hydrogen and Oxygen Evolution Reaction. *J. Colloid Interface Sci.* **2023**, *647*, 104–114.
- (48) An, L.; Zhu, J.; Yang, J.; Wang, D. Tailoring the d-band Center of Iridium-Doped Cobalt Selenide for Dual-Boosted Hydrogen and Oxygen Evolution Reactions. *Nano Mater. Sci.* **2024**, DOI: 10.1016/j.nanoms.2024.01.011.
- (49) Li, H.; Du, Z.; He, F.; Chen, S.; Yang, H.; Tang, K. Cobalt Carbonate Hydroxide Assisted Formation of Self-Supported CoNi-
- Based Metal-Organic Framework Nanostrips as Efficient Electrocatalysts for Oxygen Evolution Reaction. *Int. J. Hydrogen Energy* **2023**, *48* (41), 15566–15573.
- (50) Malik, B.; Sadhanala, H. K.; Aziz, S. T.; Majumder, S.; Konar, R.; Gedanken, A.; Nessim, G. D. Synergy between Cobalt-Chromium-Layered Double Hydroxide Nanosheets and Oxidized Carbon Nanotubes for Electrocatalytic Oxygen Evolution. *ACS Appl. Nano Mater.* **2022**, *5* (3), 4091–4101.
- (51) Zhou, Y.; Guan, P.; Chen, F.; Feng, Z.; Jia, H.; Liang, T.; Li, M.; Wan, T.; Tian, R.; Han, Z.; Chu, D. Engineering Work Functions of Cobalt-Doped Manganese Oxide Based Electrocatalysts for Highly Efficient Oxygen Evolution Reaction. *J. Colloid Interface Sci.* **2023**, *642*, 23–28.
- (52) Wen, S.; Chen, G.; Chen, W.; Li, M.; Ouyang, B.; Wang, X.; Chen, D.; Gong, T.; Zhang, X.; Huang, J.; Ostrikov, K. K. Nb-Doped Layered FeNi Phosphide Nanosheets for Highly Efficient Overall Water Splitting under High Current Densities. *J. Mater. Chem. A* **2021**, *9* (15), 9918–9926.
- (53) An, L.; Feng, J.; Zhang, Y.; Wang, R.; Liu, H.; Wang, G. C.; Cheng, F.; Xi, P. Epitaxial Heterogeneous Interfaces on N-NiMoO₄/NiS₂ Nanowires/Nanosheets to Boost Hydrogen and Oxygen Production for Overall Water Splitting. *Adv. Funct. Mater.* **2019**, *29* (1), No. 1805298.
- (54) Wang, G.; Huang, J.; Chen, G.; Chen, W.; Song, C.; Li, M.; Wang, X.; Chen, D.; Zhu, H.; Zhang, X.; Ostrikov, K. K. In-Situ-Engineered 3D Cu₃Se₂@CoSe₂-NiSe₂ Nanostructures for Highly Efficient Electrocatalytic Water Splitting. *ACS Sustainable Chem. Eng.* **2020**, *8* (46), 17215–17224.
- (55) Wang, Y.; Li, X.; Zhang, M.; Zhang, J.; Chen, Z.; Zheng, X.; Tian, Z.; Zhao, N.; Han, X.; Zaghib, K.; et al. Highly Active and Durable Single-Atom Tungsten-Doped NiS_{0.5}Se_{0.5} Nanosheet@NiS_{0.5}Se_{0.5} Nanorod Heterostructures for Water Splitting. *Adv. Mater.* **2022**, *34* (13), No. 2107053.
- (56) Ding, X.; Xia, Y.; Li, Q.; Dong, S.; Jiao, X.; Chen, D. Interface Engineering of Co(OH)₂/Ag/FeP Hierarchical Superstructure as Efficient and Robust Electrocatalyst for Overall Water Splitting. *ACS Appl. Mater. Interfaces* **2019**, *11* (8), 7936–7945.
- (57) Hui, L.; Xue, Y.; Jia, D.; Yu, H.; Zhang, C.; Li, Y. Multifunctional Single-Crystallized Carbonate Hydroxides as Highly Efficient Electrocatalyst for Full Water Splitting. *Adv. Energy Mater.* **2018**, *8* (20), No. 1800175.
- (58) Yu, M.; Budiyanto, E.; Tüysüz, H. Principles of Water Electrolysis and Recent Progress in Cobalt-, Nickel-, and Iron-Based Oxides for the Oxygen Evolution Reaction. *Angew. Chem., Int. Ed.* **2022**, *61* (1), No. e202103824.